A simple method to account for topography in the radiometric correction of radar imagery

G. LECLERC and N. BEAULIEU

Centro Internacional de Agricultura Tropical (CIAT), A.A. 6713, Cali, Colombia.

Tel:650-833-6625. Fax: 650-833-6626. Internet: g.leclerc@cgiar.org

F. BONN

Centre d'Applications et de Recherche en Télédetection,

Université de Sherbrooke, Sherbrooke, P. Québec, Canada.

Abstract. This article presents a method that allows to study and correct the radiometric distortions caused by topography in SAR images. The method is easy to implement, and requires neither sophisticated software nor code-level programming. It also considers the case of a flat surface having an elevation different from the one for which calibration parameters were derived. An ortho-image of the slant range distance is used with a digital elevation model to generate images of the local incident angle along the range and azimuth directions. The method compensates for variations in the terrain area of each pixel and for the angular dependence of backscatter, allowing the choice of either an empirical or semi-empirical scattering model. The method is applied to high-resolution C-SAR subsets of an agricultural area in the Central Cordillera of Costa Rica. The removal of topographic

features appears excellent for local incident angles up to 80°, but small-scale structures have pronounced effects on the radar return for higher local incident angles and are not adequately corrected.

Short title: Correction of relief-induced radiometric distortions of SAR imagery.

1. Introduction

Given its strong sensitivity to topography, radar remote sensing has been thoroughly used in geomorphology, and applying this technique to the study of vegetation has been largely restricted to areas with smooth topography. Also, most studies focusing on the potential of radar remote sensing for agricultural applications have taken place in developed countries where the agricultural fields are usually large and uniform, resulting from Green Revolution mechanization and optimization ideas. In Central America, however, more than 65% of agricultural land is located in mountainous areas, and rough topography combined with small plots strongly obstructs the use of radar remote sensing for crop monitoring.

The effects of oblique view and topography in a radar image include a strong geometric distortion that affects textural analysis and the precision of cartography. It also strongly modulates the radar intensity related to the variations in the angle with which the electromagnetic pulses reach the surface. If absolute calibration has been, or is to be, performed then elevation also has to be considered (see 2.4.4). When a flat surface is at an elevation different from that for which calibration parameters have been derived, a "topographic" adjustment must also be considered. For adequate

orthrectification of the terrain presenting some kind of slope, the geometrical relationship between the sensor and the surface must be considered. This in turn requires knowledge of the trajectory and look-angle of the sensor, and a Digital Elevation Model (DEM). This geometric information can then be used to adjust the radiometry for topographic effects.

At present, some commercial image-processing packages offer the possibility of precisely orthorectifying radar images using a DEM, including the radar modules of EASI/PACE (PCI, Inc.), EARTHVIEW (Atlantis Scientific Systems Group, Inc.), and SRIT (Toutin *et al.* 1992). For the radiometric correction of topographic effects, specific programs have been developed in research centers and universities (Teillet *et al.* 1985, Hinse *et al.* 1988, Bayer *et al.* 1991, Wivell *et al.* 1992, Beaudoin *et al.* 1994, Werner *et al.* 1994), but to date we know of neither public domain nor commercial packages offering this capacity. On the other hand, within the radar analysis package of EASI/PACE or EARTHVIEW, a simulated radar image can be constructed from an ortho-image and a DEM (PCI 1997, EARTHVIEW 1997). This image can be used to carry out radiometric normalization, in the same way that an artificially illuminated DEM can be used to correct an image in the optical domain. However, this method gives no control over the illumination parameters. EASI/PACE's SARSIM1 and SARSIM2 programs (PCI 1997), for instance, simulate a SAR image using a resampling trick to approximate a gain factor of $1/\sin(\theta_r)$ (which accounts for the slant-range scale compression), θ_r being the local incident angle in the range direction (Guindon and Adair 1992).

This paper aims to introduce a simple solution to account for the radiometric effects related to the slant-range projection (and thus to topography) in a SAR image. We explain how any basic raster GIS or Image Processing software can be used to generate an image of the incident angle, which in turn is combined with a DEM to correct the dependence of the radar return on topography.

A backscattering angular dependence model is then introduced to better isolate target response. The approach is to simulate the radar image that would have been obtained had the terrain been flat and at a reference altitude, therefore seeking to compensate the radiometric effects of topography, but not those of the variation of incident angle along the image swath. This is achieved through normalizing the image by what is expected from the same terrain with a given backscatter angular dependence.

2. Methodology

The method we present involves three steps. First, we calculate the viewing geometry parameters in the cartographic reference (e.g. UTM), including the incident angle $\theta_i(x,y)$, the angle between the incident electromagnetic wave vector and the vertical at the terrain surface. Then we calculate the local incident angle, the angle between the incident electromagnetic wave vector and the terrain normal, in range ($\theta_r(x,y)$) and azimuth ($\theta_a(x,y)$) directions, which depends on the topography and on the platform trajectory and look directions. Last, we make the radiometric correction. This involves applying a gain factor, which compensates variations in the terrain area of each pixel, as well as the angular dependence of backscatter.

2.1. *Computing the viewing geometry parameters in the cartographic reference*

Some methods found in the literature involve projecting the DEM along the slant and range axes of the images (Beaudoin *et al.* 1994, Castagnas *et al.* 1997, Holecz *et al.* 1994, Small *et al.* 1998). The method we describe is carried through in the cartographic projection of the DEM. The first step is to orthorectify the SAR slant-range image, which removes geometric distortions and registers it to the DEM. Note that for flat relief, it may be sufficient to use rubber sheeting procedures standard to all image processing software. During this process, the image is rotated and its pixels shifted in the range direction, according to the topography's severity (figure 1 a and b). The incident angle, i.e. the angle between the incident wave front and the vertical axis at the terrain surface, is the basic parameter needed to perform any analysis of the SAR radiometry. It is relatively complicated to obtain for the cartographic reference, since it requires calculating the distance between the sensor and a pixel to the ground as a function of the trajectory of the platform and of the geographical coordinates.

Calculating the incident angle in the cartographic reference is simplified by keeping track of the slant-range distance for each pixel during orthorectification, in the following way: a synthetic image is created in the slant-range projection, having the same dimensions as the radar image being studied, in which the Digital Number (*DN*) of each pixel *(i, j)* is proportional to the slant-range distance *SLR(i, j)* which, in slant-range images, is a linear function of the column number *j*. The resulting image has a gradation of intensity that increases linearly from near to far range (figure 1 c). The image is registered *with the same parameters* used to orthorectify the radar image. This results in a orthorectified synthetic image being created in which, for each pixel in ground range coordinates

(x,y), the slant range *SLR(x,y)* is given by its *DN* (figure 1 d). This new ortho-image is used to obtain other parameters needed for the radiometric analysis.

Knowing the viewing geometry and the slant range, we can calculate the *incident angle with respect to the vertical* at the surface of the terrain $\theta_i(x,y)$ for each pixel. We consider the simple case of an airborne sensor of constant altitude *ALTI* (figure 2). To calculate the local incident angle for spaceborne platforms, refer, for the ERS case, to Van Zyl *et al.* (1993), to Laur (1992) and to Beaudoin *et al.* (1994) and, for RADARSAT, to Shepherd (1997).

Equation 1 (see Fig. 2a) is used to calculate $\theta_i(x,y)$ from the slant range *SLR(x,y)* and the terrain elevation *H(x,y)* at pixel *(x,y)*, for airborne images.

$$\theta_i(x,y) = \cos^{-1}\left[\frac{ALTI - H(x,y)}{SLR(x,y)}\right] \qquad (1)$$

The image of θ_i (figure 3a) is used in step 2.2 below to compute the local incident angle, and is essential in itself to study the backscattering by vertical elements such as trees and certain crops. $\theta_i(x,y)$, computed for a horizontal flat surface at a reference elevation, is used for image normalization as described in section 2.4.

2.2. Computing local incident angle

Because the distances on the original slant-range and projected ground-range images are differently related to each other in the range and azimuth directions, we will consider these two axes separately and compute the corresponding components of the local incident angle (see figure 2). We must first compute the terrain slope in these two directions. This can be achieved by using commands

included in standard raster Geographical Information Systems (GIS) for terrain analysis. They allow us to calculate the maximum terrain slope $S(x,y)$ with respect to a horizontal plane, and the *aspect* $A(x,y)$ of the terrain (direction of maximum slope in the horizontal plane), clockwise with respect to the geographical north (see Fig. 2c).

We can simplify the three-dimensional representation of the terrain with respect to the sensor two dimensions by conceiving terrain normal at any pixel (x,y) as a vector **T** which orientation is given in spherical coordinates by the angles $(\phi, \theta) = (S(x,y) , A(x,y))$ (Figure 2a). Terrain slope in any direction θ can be determined by projecting **T** onto the vertical plane oriented along θ. The terrain slope in that direction is given by the angle that the projected **T** makes with the vertical. In this way we can calculate $S_r(x,y)$, the terrain slope in the range direction, from the maximum slope $S(x,y)$ and aspect $A(x,y,)$ of the terrain and the platform's flight direction (i.e. heading *HEAD* – see figure 2a).

In this case the plane we project **T** onto is called the incidence plane, and its orientation is perpendicular to *HEAD*.

For right-looking images:

$$\tan[S_r(x,y)] = \tan[S(x,y)] \cdot \cos[A(x,y) - (HEAD + 90)] \qquad (2)$$

where *HEAD* and $A(x,y)$ are expressed in degrees. Note that slopes facing the antenna direction are negative.

In the range direction, the local incident angle $\theta_r(x,y)$ (figure 2a, 3b) is the sum of the incident angle $\theta_i(x,y)$ and the terrain slope in the range direction $S_r(x,y)$:

$$\theta_r(x, y) = S_r(x, y) + \theta_i(x, y) \qquad (3)$$

The image of θ_r can be used to build *approximate* shadow and layover masks: areas with θ_r greater that 90° will be shadow areas (although this does not account for cast shadows), and the ones with negative θ_r will suffer from layover.

In the azimuth direction, the local incident angle $\theta_a(x,y)$ (figure 2b, 3c) is simply given by the terrain slope in the azimuth direction (i.e. $\theta_a(x,y)=S_a(x,y)$):

$$\tan[\theta_a(x, y)] = \tan[S(x, y)] \cdot \cos[A(x, y) - HEAD] \qquad (4)$$

The parameters $\theta_i(x,y)$, $\theta_r(x,y)$, and $\theta_a(x,y)$ form separate layers of a GIS (as in Bayer *et al.*, 1991) that can be used to make a semi-empirical analysis of the radar backscattering using only pixel by pixel arithmetic operations. Note that this decomposition in range and azimuth is valid even for systems with a squint angle, where range and azimuth directions are not completely perpendicular.

2.3. Alternative method to calculate the local incident angle

When the particular parameters of the viewing geometry (such as *ALTI* or *HEAD*) are not known, or the geometry cannot be simply modeled (such as in the satellite case over wide coverage,

or airborne in windy conditions), $\theta_i(x,y)$, $\theta_r(x,y)$, and $\theta_a(x,y)$ can still be computed using a method developed by Leclerc and Beaulieu (1996). As pointed out by Van Zyl *et al* (1993), an error in the estimation of the flight altitude can introduce important errors in the calculation of the incident angle. We know that the ground range is a function of the slant range, which is modulated by terrain effects. Thus the ortho-image of the slant-range distance, $SLR(x,y)$, contains all the information needed on the viewing geometry. It can be shown (Leclerc and Beaulieu, 1996) that $SLR'(x,y)$, the change of $SLR(x,y)$ with respect to displacements in the cartographic reference (i.e. x and y) - the derivative of SLR - _, is directly related to $\theta_r(x,y)$ and $S_r(x,y)$, as given by equation 5:

$$\sin[\theta_r(x,y)] = SLR'_r(x,y) \cdot \cos[S_r(x,y)] \qquad (5)$$

where $SLR'_r(x,y)$ is the projection, in the range direction, of the derivative $SLR'(x,y)$ of the ortho-image of the slant-range $SLR(x,y)$. This derivative can be calculated using a standard raster GIS command to compute slope. $SLR'_r(x,y)$ is obtained in the same way as S_r in equation 2. Then $\theta_i(x,y)$ is computed from equation 3.

HEAD , if unknown, can also be derived directly from the ortho-image $SLR(x,y)$. In effect, most of the distortion of a slant-range image is in the range direction, and influences the *aspect* (direction of maximum slope) of $SLR(x,y)$. When topography is significant, however, the *aspect* of $SLR(x,y)$ can differ a lot from the range direction. Therefore, to estimate *HEAD* one can compute the histogram of the *aspect* image of $SLR(x,y)$ (which is calculated by applying the corresponding standard raster GIS command) in a portion of the image with relatively flat terrain; the mean value of the *aspect* obtained (or median if preferred) corresponds to the range direction, which allows to

compute HEAD, taking in consideration the SAR squint angle.

Using this method, one must work with 32-bit real numbers to capture the subtle variations in *SLR(x,y)*. The accuracy of the method is totally dependent on that of the georeferencing.

2.4 Radiometric correction

The radiometric correction described in the following paragraphs compensates for variations in the terrain area of the pixels (i.e., the scattering area contributing to the brightness of image pixels) and for the angular dependence of backscattering. The approach is to simulate the radar image that would have been obtained had the terrain been flat and at a reference altitude, assuming the surface obeys a given backscattering angular model. Using calibration parameters, when available, we can take into account system-dependent gain factors such as antenna pattern, gain compensation, and noise power affecting the *DN*. This allows us to calculate σ^0, the backscattering coefficient, or backscattering cross-section per unit area on the ground. Note that calibration procedures are developed for flat (or curved) terrain at a reference elevation, so the compensation of the previously mentioned effects has to be conducted in function of this hypothetical surface.

2.4.1. Variation of the terrain scattering area

To compute σ^0 in function of the *DN* in digital images, we have to compensate for the variation of the terrain area contributing to the brightness of an image pixel (Laur 1992, Van Zyl *et al.* 1993, Fiksel *et al.* 1994, Hoekman *et al.* 1994, Ulander *et al.* 1994, Werner *et al.* 1994, Ulander 1995). Even for satellite images that are usually delivered in a ground-range geometry, the sampling intervals and the size of the resolution cell are constant only in the initial image acquired in the slant-range geometry. Brightness in a slant-range image pixel is determined by the signal received from

an area on the ground that depends on θ_r. It is proportional to σ^0 times the scattering area on the ground. Explicitly, this area is $[sin(\theta_r).cos(\theta_a)]^{-1}$ times larger than the corresponding area in the slant range image, even when the squint angle is non-zero and azimuth and range directions are not perpendicular. (In the range direction, the ratio between the length of a resolution cell in the slant-range projection and its corresponding length in ground range is $sin(\theta_r)$, while in the azimuth direction, the ratio between the width the resolution cell in the slant range projection and its corresponding width in the ground range projection is $cos(\theta_a)$, because the positions are projected vertically.)

This variation in scattering area caused by topography induces important variations in the radiometry of a slant-range image, and tends to dominate for steep viewing (small θ_r). By taking this effect into account, one can turn raw brightness (proportional to the energy measured for a given slant-range pixel area) into images of local brightness (energy per unit of terrain area), even when complete calibration is not the issue.

2.4.2. *Backscattering models*

Having taken into account the effect of varying terrain area, one can choose a model that describes the target's backscattering angular dependence. Such a model may be obtained through the fit of an arbitrary function to the image data, with $\theta_i(x,y)$, $\theta_r(x,y)$, and $\theta_a(x,y)$ as independent variables (Itten and Meyer 1993). One may otherwise fit a specific angular dependence of the scattering function (Teillet *et al.* 1985, Wivell *et al.* 1992, Bayer *et al.* 1991). The angular behavior of back scattering varies with wavelength and surface geometry, and thus will be different for different land uses. A model presented here corresponds to scattering by a lambertian surface (producing equal

diffusion in all directions and no absorption) following the same topography as the studied terrain. Although in nature few surfaces behave as truly lambertian surfaces, using this ideal behavior in normalization allows to examine the *deviation* of actual scattering with respect to lambertian scattering. This offers valuable insights on the type of scattering involved. It highlights the angular behavior of both the elastic scattering and absorption, both of which are characteristic of a particular target.

Let us examine the energetics involved for a lambertian scatterer. The incident irradiance (incident flux per unit area) that reaches an inclined surface is equal to the irradiance that a surface perpendicular to the incident wave front would have received, multiplied by [$\cos(\theta_r)$ $\cos(\theta_a)$], which is the projection of the terrain unit surface on the wave front. In other words, the energy received on terrain unit area changes with the local incident angle. If the wave front were totally reflected back to the antenna, σ^0 would follow a simple cosine law. For a perfectly rough surface, the wave front is not totally reflected, but is dispersed in function of a cosine law, implying another [$\cos(\theta_r)$ $\cos(\theta_a)$]. In this case, σ^0 will follow a square cosine law.

For a *lambertian* surface, the backscattering coefficient per unit terrain surface is given by:

$$\sigma_L^0 = \sigma_0^0 \cdot \cos^2[\theta_r(x,y)] \cos^2[\theta_a(x,y)] \qquad (6)$$

where σ_0^0 is a constant (= 2 in the elastic scattering situation, according to Ulaby *et al.* 1986).

Many authors suppose a $cos(\theta)$ dependence for σ^0 (Mougin *et al.* 1994, Beaudoin *et al.* 1994, Hawkins and Teany 1994). Although this implies a surface that is rougher than lambertian, this seems to better describe the angular dependence of the scattering in C-VV over tropical rainforest for

incident angles between 20° and 60°. For this case we would use the *independent gamma* cross-section:

$$\sigma^0_{IG} = \sigma^0_0 \cdot \cos\left[\theta_r(x,y)\right] \cos\left[\theta_a(x,y)\right] \qquad (7)$$

Another interesting case is the *independent backscattering* cross-section, $\sigma_{IB}{}^0 = \sigma_0{}^0$, which corresponds to the distributed independent point reflector (Ulaby *et al.* 1986).

These three models will be referred to in the following paragraphs as lambertian (L), independent gamma (IG), and independent backscattering (IB). Clapp (1946) describes them and Cosgriff *et al.* (1960) and Ulaby *et al.* (1986) refer to them. Note that it is unlikely that a single model will do for any land cover present in the image, and that we cannot a priori favor one model over another. The user is free to choose or derive the model that better describes the backscattering for a particular area of interest. All three models and intermediate situations can be described by the general equation:

$$\sigma^0_n = \sigma^0_0 \cdot \left[\cos\left[\theta_r(x,y)\right] \cos\left[\theta_a(x,y)\right]\right]^n \qquad (8)$$

where n=2 for the lambertian case, 1 for the independent gamma and 0 for independent backscattering. Note that the case n=0 results in correcting only the effect of variations in scattering area.

2.4.3. General form of intensity image

Equation 9 therefore gives the effect of local incident angle on the DN stored in a slant-range

pixel (DN is proportional to backscatter amplitude) without noise.

$$DN^2(x,y) = \frac{k(x,y)\cdot\sigma^0(x,y)}{\sin[\theta_r(x,y)]\cos[\theta_a(x,y)]} \qquad \theta_r, \theta_a < 90^\circ$$

$$DN^2(x,y) = 0 \qquad \theta_r \geq 90^\circ \tag{9}$$

where $k(x,y)$ is the proportionality factor that takes into account the system-dependent factors. It should be pointed out that areas with θ_r greater than 90° are shade areas, so that any signal in these areas can be attributed to noise.

For the models described above we obtain:

$$DN_n^2(x,y) = \frac{k(x,y)\cdot\sigma_0^0\cdot\cos^n[\theta_a(x,y)]\cos^n[\theta_r(x,y)]}{\sin[\theta_r(x,y)]\cos[\theta_a(x,y)]}$$

$$= k(x,y)\cdot\sigma_0^0\cdot\cot[\theta_r(x,y)]\cdot[\cos[\theta_a(x,y)]\cos[\theta_r(x,y)]]^{n-1} \quad \theta_r, \theta_a < 90^\circ \tag{10}$$

n=0 for IB, 1 for IG, 2 for L

2.4.4. *Eliminating topographic effects*

SAR systems are calibrated for ground surfaces at a reference elevation, H_{ref}. For example, in the case of ERS-1 images, the reference elevation corresponds to the GEM6 ellipsoid, according to Laur (1992). Any surface at an elevation other than H_{ref} will contain some radiometric distortion because the incident angle at a given (x,y) position varies with the elevation. The larger the difference between the terrain and H_{ref} relative to the antenna altitude, the greater the distortion.

Our interest here is to develop a correction for the topographic effects only, leaving the image

untouched if the corresponding terrain is flat and at an H_{ref} elevation. An image of $\frac{DN_{model}(x,y)}{DN_{model}(x,y)|_{H_{ref}}}$ will have the required qualities as a correction factor, being equal to one except where the terrain is not flat and is at an elevation different from H_{ref}. By doing this, we also eliminate σ_0^0, and $k(x,y)$, the system-dependent calibration parameter (see equation 14). The image with topographic effects removed, $DN_{cor}(x,y)$, is therefore obtained by dividing the raw image by the image of $\frac{DN_{model}(x,y)}{DN_{model}(x,y)|_{H_{ref}}}$ for a given model. The range-dependent noise, if significant, can be removed before normalization.

According to equation 9, the expected model backscattering for a flat terrain at an elevation H_{ref} is given by:

$$DN^2(x,y)\,|_{H=H_{ref}} = k(x,y)\cdot\frac{\sigma^0(x,y)|_{H_{ref}}}{\sin[\theta_i(x,y)|_{H_{ref}}]} \qquad (11)$$

$$DN_n^2(x,y)\,|_{H=H_{ref}} = k(x,y)\cdot\sigma_0^0\cdot\cot[\theta_i(x,y)|_{H_{ref}}]\cdot\left[\cos[\theta_i(x,y)|_{H_{ref}}\right]^{n-1} \qquad (12)$$

Explicitly, the corrected image is obtained as:

$$DN_{cor}(x,y) = \left\{ \frac{DN_{model}^{\ 2}(x,y)_{|H_{ref}}}{DN_{model}^{\ 2}(x,y)} \cdot \left[DN^2(x,y) - DN_n^{\ 2}(x,y) \right] \right\}^{1/2} \qquad \theta_r, \theta_a < 90°$$

(13)

$$DN_{cor}(x,y) = 0 \qquad \theta_r \geq 90°$$

where $DN_n^2(x,y)$ is the range-dependent noise power that, if not previously determined during calibration procedures, can be estimated by using shadow areas in the image.

We therefore have:

$$DN_{cor,n}(x,y) = \left\{ \frac{\tan[\theta_r(x,y)]}{\tan[\theta_i(x,y)|_{H_{ref}}]} \cdot \left[\frac{\cos[\theta_i(x,y)|_{H_{ref}}]}{\cos(\theta_r).\cos(\theta_a)} \right]^{n-1} \left[DN^2(x,y) - DN_{noise}^{\ 2}(x,y) \right] \right\}^{1/2}$$

(14)

where n=0 for IB, n=1 for IG, n=2 for L.

The correction diverges as θ_r and θ_a approach 90° (see figure 4b which illustrates the lambertian case). The divergence rate is also much greater in the range direction than in the azimuth direction.

2.4.5. Antenna pattern correction and absolute calibration

An image corrected using equation 14 will be substantially flattened radiometrically, and therefore more suitable for an empirical antenna-pattern and noise-power correction (based on averaging the DN of a given slant range). When applied to raw images, this method does not give good results in mountainous areas, especially if ridges are parallel to the flight line: scene-dependent

effects remain that greatly reduce the quality of the antenna pattern correction. Because system-dependent radiometric distortions (such as antenna pattern or noise power) are principally functions of the slant range, we can use the layer *SLR(x,y)* as the independent variable and determine the antenna pattern correction or noise power with the normalized image.

With the users growing interest in calibrated satellite images, software vendors now include routines to calculate σ° in their radar package. Calibration accounts for system dependent parameters such as gain factors (k) or noise (DN_n^2), and in some cases compensates the change of ground pixel size for flat terrain at reference elevation (which depends on $\sin(\theta_i)|_{H_{ref}}$). The correction coefficients developed above (Equation 14) are directly applicable to calibrated images, in the way that the image is left untouched if the terrain is flat and at the reference elevation. If the calibrated image to be radiometrically corrected for topography is one of $\sigma^{0}{}_{cal}$, the backscattering coefficient calculated supposing a flat surface at a reference elevation. The correction for topography is therefore:

$$\sigma^{\circ}{}_{cor,n}(x,y) = \left\{ \frac{\tan[\theta_r(x,y)]}{\tan[\theta_i(x,y)|_{H_{ref}}]} \cdot \left[\frac{\cos[\theta_i(x,y)|_{H_{ref}}]}{\cos(\theta_r).\cos(\theta_a)} \right]^{n-1} \cdot \sigma^{0}{}_{cal}(x,y) \right\} \qquad (15)$$

Application

We have applied our method to C-SAR slant-range image subsets near the town of Juan Viñas, in the central cordillera of Costa Rica. The acquisition of flight lines 8.2 and 8.3 was planned by *Proyecto Radar Costa Rica Canada*, as a complement to the SAREX mission in Latin America (Ahern *et al.* 1994, Wooding *et al.* 1994). The imagery was acquired on April 27th, 1992 in C band,

narrow-mode, and HH and VV polarizations, with the C-SAR system aboard the Convair 580 of the Canadian Center of Remote Sensing (CCRS). For this mode, resolution is 6 m × 6 m, with a pixel size of 4 m in slant range and 4.31 m in azimuth. The imagery covers the study area with different incident angles and opposite look-directions. Fieldwork was conducted simultaneously with the image acquisition, providing an extensive database and a collection of videos and hand-held 35-mm photos taken from a small airplane and from surrounding lookouts. These proved essential to analyze and interpret the radar back scattering without bias.

To geometrically correct the radar images, we used the programs FLIGHT and STGBIG, of EASI/PACE's radar module (PCI, 1997), to produce ortho-images with ± 2 m (rms) precision in X and Y, based on 23 ground control points (GCPs) taken from road intersections and field boundaries at a 1:10 000 scale. Nearest neighbor resampling was applied to preserve the radiometry of the original image. A DEM was interpolated using INTERCON, from the raster GIS IDRISI (IDRISI, 1992), from the contour lines of 1:10 000 scale topographic maps (based on 1989 airphotos, 5 m contour interval). The DEM was interpolated according to a 2 x 2 m grid; a 5 x 5 median filter was then applied to it, followed by a contraction to a 4-m x 4-m pixel, and subsequent 5 x 5 median filtering. In the radar ortho-image of the study zone corresponding to flight line 8.3 (figure 5b), one can observe that the area presents a lightly rolling relief that the canyon of the Quebrada Honda River cuts vertically. The area is covered by sugarcane on mild slopes (up to 10°) and by coffee, forest, plantain, banana, and vegetable crops on steeper slopes (15°- 40°).

3. Results

During the acquisition of the SAREX data, a procedure called Sensitivity Time Control (STC)

was applied to obtain images with flat radiometry over ground targets. Whereas images acquired in nadir mode still contained obvious range-dependent radiometric modulations, these flight lines acquired in narrow-mode had a relatively even radiometry. For this data, topographic normalization is therefore expected to give good results for analysis. The method has been implemented using standard procedures of the image processing software PCI, including the raster modeling scripting language. No code-level programming was required.

Figure 5a shows the subset of flight line 8.3 before topographic normalization using Equation 14, with H_{ref}= 0 and n=2 and figure 5b shows the subset afterwards. Ground range pixel size is the same as the DEM, i.e. 4-m x 4-m. Speckle has been removed by filtering with a morphological filter (Lira et al, 1997). We can see that the image radiometry has been substantially flattened and that departure from lambertian scattering becomes easy to track visually, especially at high (>70°) local incident angles. As Elachi (1987) points out, the radar return for high θ_r brings more information on the small-scale structure, and for low θ_r it provides information on the surface slope distribution. This is evidenced here as the slope facing the radar in the Quebrada Honda canyon, which presents low values of θ_r, shows a tone similar to the surroundings. . On these slopes we can now distinguish forest and plantain or banana plantations from coffee plantations.

In figure 5b, the area indicated by arrow is a moist, bare-soil field, recently heavily plowed, that presented a rough surface (estimated to be >25 cm rms). In the uncorrected image, we might have attributed this unusually high return to topographic effects such as those appearing in the surroundings. The radiometric correction removes the ambiguity, because the field preserves its high return and the surrounding bright areas disappear.

θ_i, θ_r, and θ_a images provide useful information for the study of radar scattering on specific

targets. For example, we found that targets as different as bare soil, and coffee and sugarcane fields appear bright for high θ_r (meaning that $DN>DN_L$) (see bright areas in figure 5b). This return, stronger than expected from a lambertian scatterer, indicates an increased effect of corner reflectors for high θ_r. This effect has a highly defined threshold in the 70°-80° range, where exact value may depend on the type of target.

Conversely, trees and buildings now show up as bright spots because they act as corner reflectors and not as lambertian targets. This somehow reduces the visual quality of the images but allows an easier detection of such components.

4. Conclusion

We have presented a straightforward method to study and correct radiometric distortions caused by topography in SAR images. The method is simple and easy to implement, and does not require sophisticated software or code-level programming. Any rectification software (with polynomial or radar-specific transformations) can be used to generate a georeferenced image of the slant range. This image, together with the DEM, is then used to generate images of the local incident angle along the range and azimuth directions. Empirical or semi-empirical scattering models can then be applied and tested against the SAR image. We derive the corrections for three angular models (independent backscattering, independent gamma, and lambertian) and extend our work to the case of calibrated images.

In the area of Juan Viñas in Costa Rica, high-resolution C-SAR image subsets have been normalized with a synthetic image assuming lambertian scattering. The removal of topographic features appeared excellent for local incident angles up to 70°. For higher local incident angles, small-

scale structures have pronounced effects in the radar return and were not corrected.

Acknowledgements

We would like to thank Alexander Salas at the Centro Agronómico Tropical de Investigación e Enseñanza (CATIE), who produced the DEM. Special thanks to Frank Ahern and Keith Raney, from CCRS, who brought us excellent technical support and useful comments. PCI, Inc. lent CATIE two full versions of EASI/PACE, without which it would have been difficult and time-consuming to conduct this study. Thanks also to Glenn Hyman, David Williams, Jetse Stoorvogel, Annie Jones, and the two anonymous referees for their detailed revision of the manuscript. The Proyecto Radar Costa Rica/Canada, coordinated by the Instituto Geográfico Nacional de Costa Rica, provided the images and a platform for interesting scientific exchanges. This study was financed by the International Development Research Center of Canada, the National Research Council of Canada, the SYNERGIE program of the Fonds de Développement Technologique du Québec, the United States Agency for International Development, and the Consultative Group for International Agricultural Research.

References

AHERN, F. J., CAMPBELL, F. H. A., ELIZONDO, C., KUX, H. J. H., NOVO, E., PARADELLA, W., RANEY, R. K., SALCEDO, R., SHIMABUKURO, Y., and SINGHROY, V., 1994, C-band SAR for Resource Management in Tropical Environments: Lessons from SAREX-92 Investigations in Brazil, Costa Rica, Venezuela, and Guyana. *Proceedings of the SAREX-92 Workshop, European Space Agency (ESA) Headquarters, Paris*, 6-8 December 1993, ESA Workshop Procs-76, pp. 41-53.

BAYER, T., WINTER, R., and SCHREIER, G., 1991, Terrain influences in SAR backscatter and attempts to their correction. *IEEE transactions on Geoscience and Remote Sensing*, **29(3)**, 451-462.

BEAUDOIN, A., DESHAYES, M., PIET, L., STUSSI, N., and LE TOAN, T., 1994, Retrieval and analysis of temperate forest backscatter signatures from multitemporal ERS-1 data acquired over hilly terrain. *Proceedings of the First ERS-1 Pilot Project Workshop, Toledo, Spain*, 22-24 June 1994 (ESA SP-365), pp. 283-289.

CASTAGNAS, L., STUSSI, N., BEAUDOIN, A. et CASTEL, T (1997). Une m/thode unifi/e de correction des images RSO acquises en terrain accidenté. Physical Measurements and Signatures in Remote Sensing, Guyot & Phlupin (eds), Balkema, Rotterdam, pp. 35-42.

CLAPP, R. E., 1946, A theoretical and experimental study of radar ground return. MIT Radiation lab, Report 6024.

COSGRIFF, R. L., PEAKE, W. H., and TAYLOR, R. C., 1960, Terrain scattering properties for sensor design (Terrain handbook II). Engineering experiment station Bulletin 181, Ohio State University.

EARTHVIEW, 1997, Command directory for EARTHVIEW version 4.4, SIMSAR program. Atlantis Scientific Systems Group Inc, Ottawa, Ontario. pp. 513-514.

ELACHI, C., 1987, *Spaceborne Radar Remote Sensing: Applications and Techniques. IEEE Press*, New York, p.12.

FIKSEL, T., HARTMAN, R., and WINZER, W., 1994, ERS-1 data for mapping of the Antarctic Peninsula by shape-from-shading technique. *Proceedings of the second ERS-1 symposium, Space at the service of the environment, Hamburg, Germany*, 11-14 October 1993. European Space Agency (ESA) SP-361, pp. 153-158.

GUINDON, B., and ADAIR, M., 1992, Analytic formulation of SAR airborne image geocoding 'value-added' and product generation procedure using digital elevation data. *Canadian J. of Remote Sensing*, **18**, 2-11.

HAWKINS, R. K., and TEANY, L. D., 1994, South American Radar Experiment (SAREX) 1992 Data Calibration. *Proceedings of the SAREX-92 Workshop, European Space Agency (ESA) (ESA) Headquarters, Paris*, 6-8 December 1993, ESA Workshop Procs.-76, pp. 41-53.

HINSE, M., GWYN, Q. H., and BONN, F., 1988, Radiometric correction of C-band imagery for topographic effects in regions of moderate relief. *IEEE Trans. Geosci. Remote Sensing*, **26**, 122-132.

HOEKMAN, D. H., VAN DER SANDEN, J. J., and BIJKER, W., 1994, Results of the SAREX-92 campaign in Guyana and Colombia. *Proceedings of the SAREX-92 Workshop, European Space Agency (ESA) Headquarters, Paris*, 6-8 December 1993, ESA Workshop Procs.-76, pp. 157-166.

HOLECZ, F., MEIER, E., PIESBERGEN, J., WEGMULLER, U., and NUESCH, D., 1994,

Radiometric Calibration of Airborne SAR Imagery. *International Geosciences and Remote Sensing Symposium* (IGARSS)'94, 1096-1098.

IDRISI, 1992, INTERCON, Intercontour interpolation. *IDRISI version 4.0 Technical reference*, 87-88.

ITTEN, K. I., and MEYER, P., 1993, Geometric and radiometric correction of TM data of mountainous forested areas. *IEEE Transactions on Geoscience and Remote Sensing*, **31(4)**, 764-770.

LAUR, H., 1992, Derivation of backscattering coefficient σ^0 in ERS-1. SAR.PRI Products. *ERS-1 SAR Calibration, ESA/ESRIN report*. October 17th. 16 pp.

LECLERC, G., and BEAULIEU, N., 1996, Two simple methods to correct radiometric distortions due to the slant-range projection in an airborne radar image. *Second International Airborne Remote Sensing Conference and Exhibition, San Francisco, California*, 24-27 June. pp. I305-I314.

LIRA, J., FERNÁNDEZ, S., and MORENO, V., 1997, Analysis de texturas en imagenes SAR. *Proceedings of the Seminario Internacional de Radar, San José, Costa Rica*, 1-5 November 1993. *(Available from Carlos Elizondo, Instituto Geográfico Nacional, San José, Costa Rica).*

MOUGIN, E., LOPES, A., HERY, P., LE TOAN, T., FROMARD, F., and RUDANT, J.-P., 1994, Multifrequency and multipolarization observations on mangrove forests of French Guyana during SAREX-92 experiment. Preliminary results. *Proceedings of the SAREX-92 Workshop*, ESA *European Space Agency (ESA)* Headquarters, Paris, 6-8 December 1993, ESA WPP-76, pp. 193-203.

PCI, 1997, On-line help documentation for FLIGHT: Flight path parameter estimation, SARSIM1:

Generate range-azimuth simulated SAR image, SARSIM2: Pseudo-geocoded SAR simulation, STG: Slant or Ground range radar data registration. *EASI-PACE version 6.2 Radar Analysis Package*.

SHEPHERD, N., 1997, Extraction of Beta Nought and Sigma Nought from RADARSAT CDPF Products. Report No AS97-5001, ALTRIV Systems, Ottawa, Canada. February 21st . 9 p.

SMALL, D., HOLECZ, F., MEIER, E. and NÜESCH, D. (1998). Absolute Radiometric Correction in Rugged Terrain; A Plea for Integrated Radar Brightness. *Proceedings of the International Geosciences and Remote Sensing Symposium (IGARSS) '98, Seattle, U.S.A, 6-10 July. IEEE, pp. 330-332.*

TEILLET, P. M., GUINDON, B., MEUNIER, J. -F., and GOODENOUGH, D. G., 1985, Slope-Aspect effects in Synthetic Aperture Radar imagery. *Canadian J. Remote Sensing*, **11,1**, 39-50.

TOUTIN, T., CARBONNEAU, Y., and ST-LAURENT L., 1992, An integrated method to rectify airborne radar imagery using DEM. *Photogrammetric Engineering and Remote Sensing*, **58(4)**, 417-422.

ULABY, F. T., MOORE, R. K., and FUNG, A. K., 1986, Microwave remote sensing, active and passive, Vol. 2, Artech House, Norwood, Massachusetts, pp. 576-577 and pp. 836-837.

ULANDER, L.M.H., 1995, A new look at the slope correction for SAR radiometric calibration. *Proceedings of the International Geosciences and Remote Sensing Symposium (IGARSS) '95, Florence, Italy*. pp. 602-604.

ULANDER, L. M. H., HAGBERG, J. O., and ASKNE, J., 1994, ERS-1 SAR interferometry over forested terrain. *Proceedings of the second ERS-1 symposium, Space at the service of the environment*, Hamburg, Germany, 11-14 October 1993, ESA SP-361, pp. 475-480.VAN ZYL,

J.J., CHAPMAN, B.D., DUBOIS, P., and SHI, J., 1993, The effect of topography on SAR calibration. *IEEE Transactions of Geoscience and Remote Sensing*, **31(5)**, 1036-1043.

WERNER, C. L., WEGMULLER, U., SMALL, D., and ROSEN, P., 1994, Applications of interferometrically derived terrain slopes: normalization of SAR backscatter and the interferometric correlation coefficient. *Proceedings of the second ERS-1 symposium, Space at the service of the environment*, Hamburg, Germany, 11-14 October 1993. ESA SP-361, pp. 723-726.

WIVELL, C. E., STEINWAND D. R., KELLY, G. G., and MEYER, D. J., 1992, Evaluation of terrain models for the geocoding and terrain correction of SAR Images, *IEEE transactions on Geoscience and Remote Sensing*, **30(6)**, 1137-1144.

WOODING, M. G., ZMUDA, A. D., and ATTEMA, E., 1994, An overview of SAREX-92 data acquisition and analysis of the tropical forest environment. *Proceedings of the SAREX-92 Workshop, European Space Agency (ESA)* ESA Headquarters, Paris, 6-8 December 1993, ESA WPP-76, pp. 41-53.

Figure captions

Figure 1: The synthetic image of the slant range *SLR(x,y)* (figure 1c), is orthorectified (figure 1d) with the same parameters as those used to produce the radar ortho-image (figures 1a – north is towards the bottom of the page - and 1b).

Figure 2: Geometry of an airborne, right-looking radar (constant altitude *ALTI*):
(a) Representation of terrain normal **T** and its projection on the incidence plane (the projected vector makes an angle S_r with the vertical) and on the azimuth plane (the projected vector makes an angle S_a with the vertical). S is the maximum terrain slope, and A the direction of the maximum slope. These angles define the orientation of terrain normal at coordinate *(x,y)*.
(b) Geometry in the incidence plane , (c) Geometry in the azimuth plane.

Figure 3: Calculated images of: (a) θ_i, the incident angle with respect to the vertical, (b) θ_r, the local incident angle in the range direction, and (c) θ_a, the local incident angle in the azimuth direction.

Figure 4: Graphs showing (a) the dependence on the DN_L(proportional to the backscatter amplitude), and (b) the inverse of DN_L (proportional to the correction factor) on the local incident angle in the range and azimuth direction (see Equation 10 with n=2) for lambertian scattering.

Figure 5: High-resolution C-SAR ortho-images of the Juan Viñas area, Costa Rica: (a) raw image (HH = Red, VV = Cyan); (b) radiometrically corrected for the topography using Equation 14, with $H_{ref} = 0$.

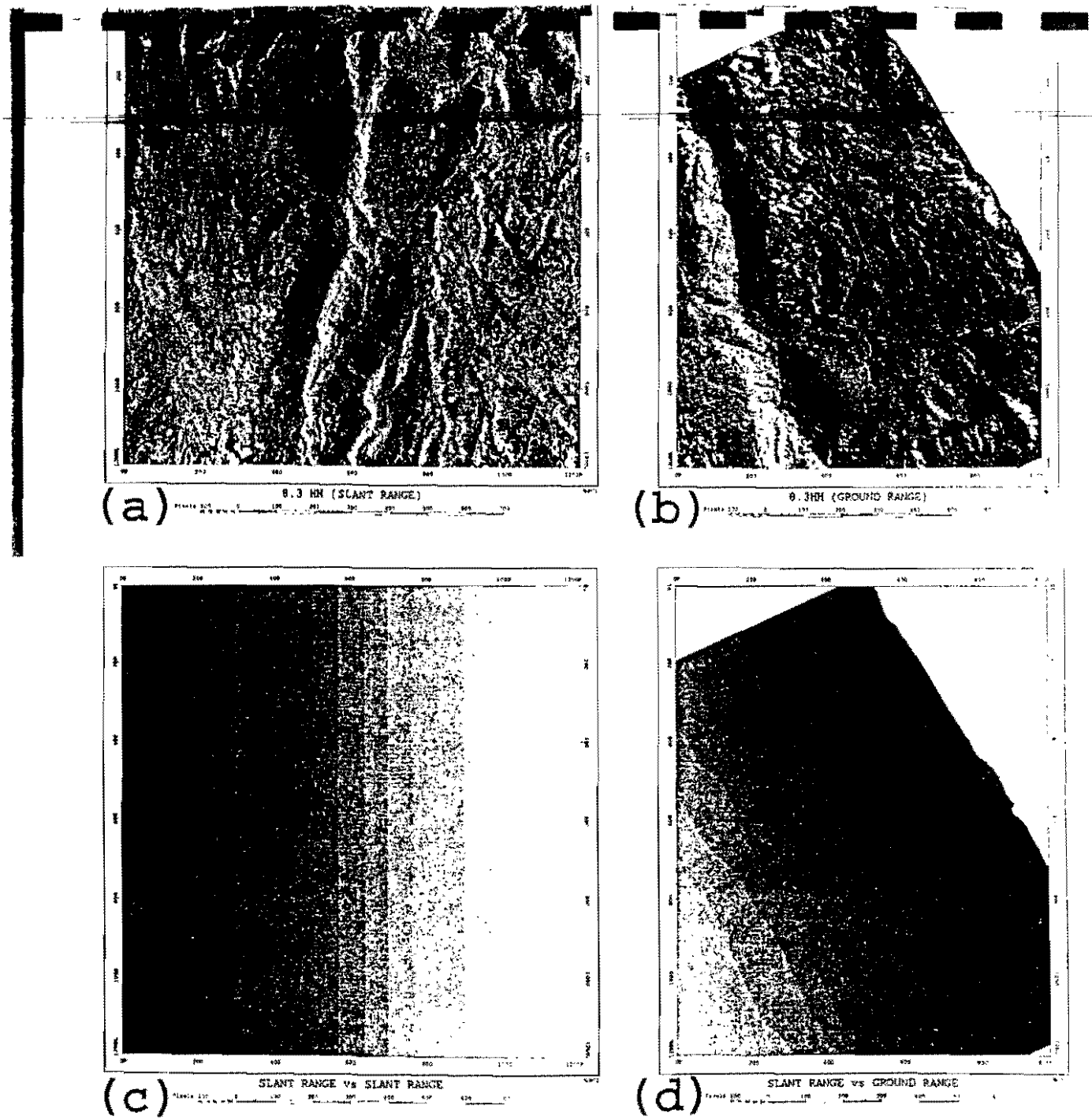
(a)
0.3 HH (SLANT RANGE)
(b)
0.3HH (GROUND RANGE)
(c)
SLANT RANGE vs SLANT RANGE
(d)
SLANT RANGE vs GROUND RANGE

Figure 1

(a)

(b)

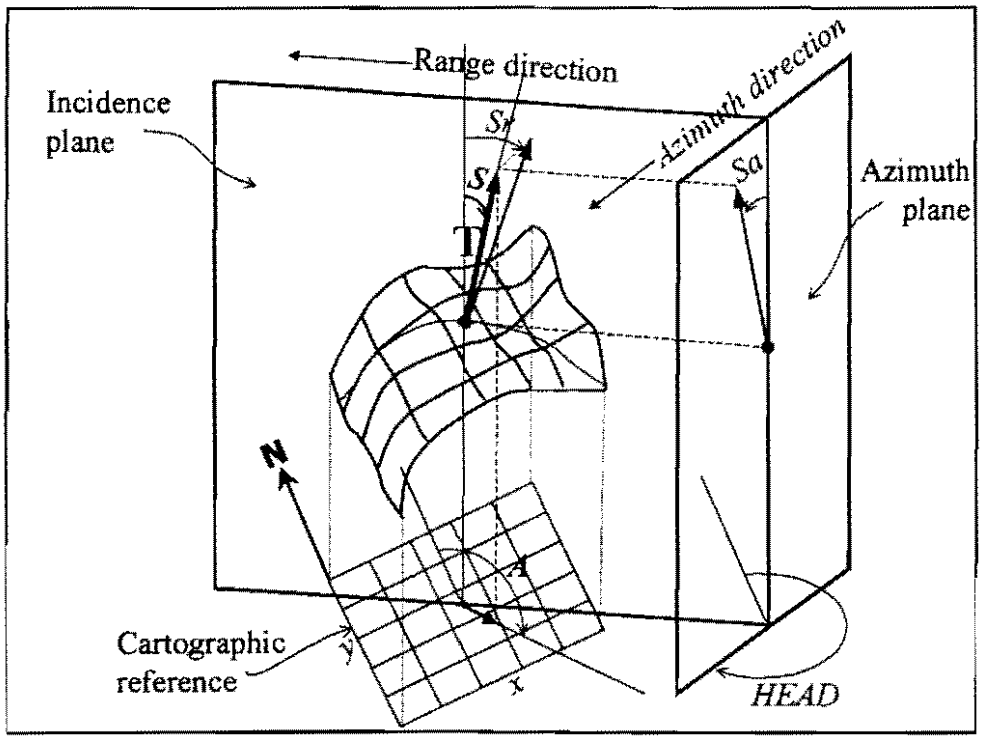
Range direction
Incidence plane
Azimuth direction
Sr
S
Sa
Azimuth plane
T
N
A
Cartographic reference
y
x
HEAD

(c)

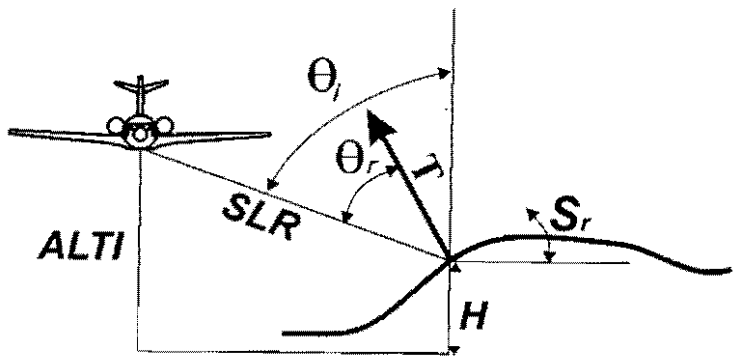
θi
θr
T
SLR
ALTI
Sr
H

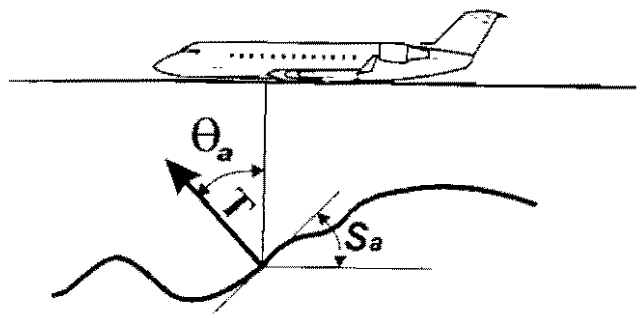
θa
T
Sa

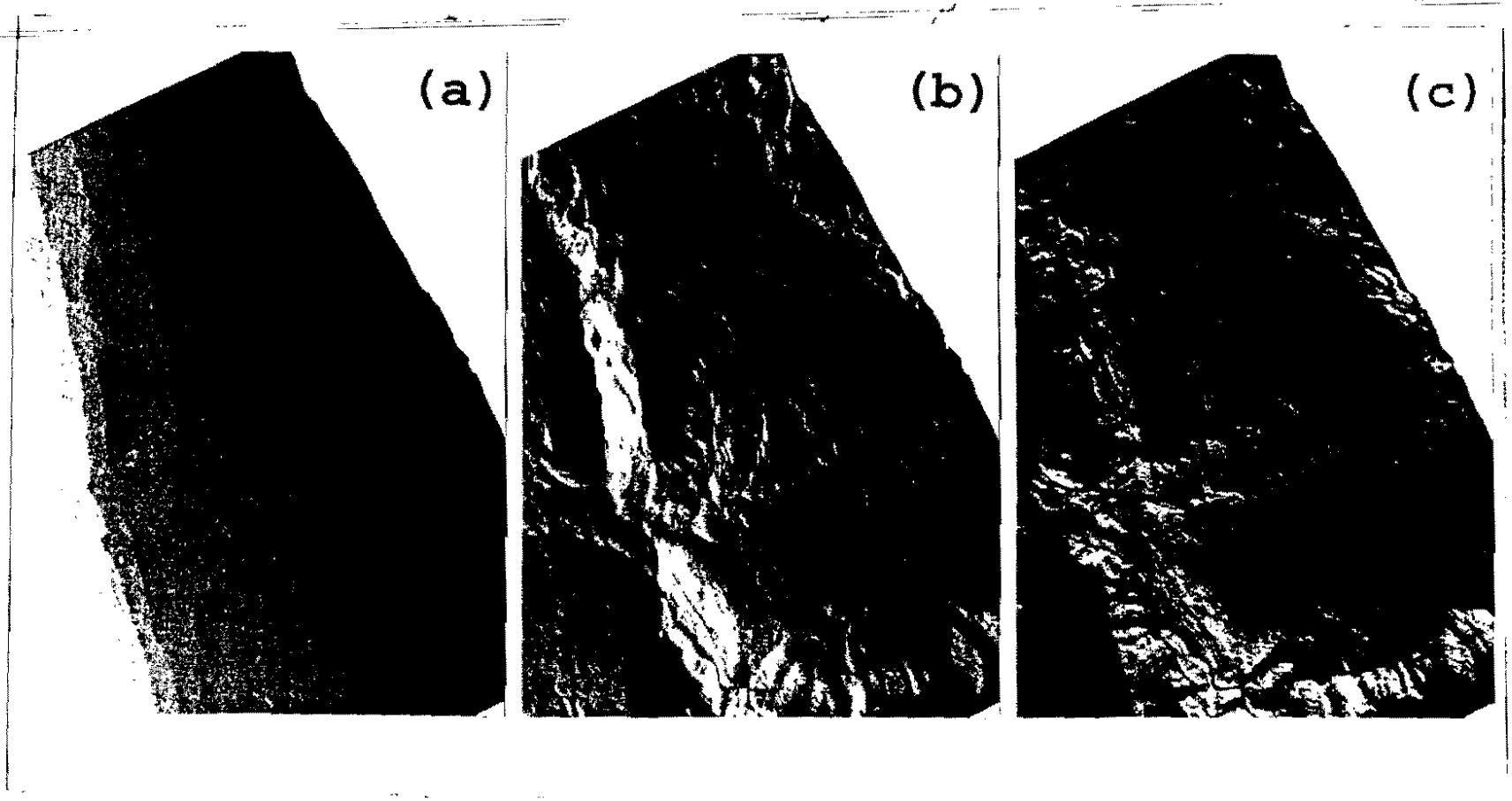

Figure 3

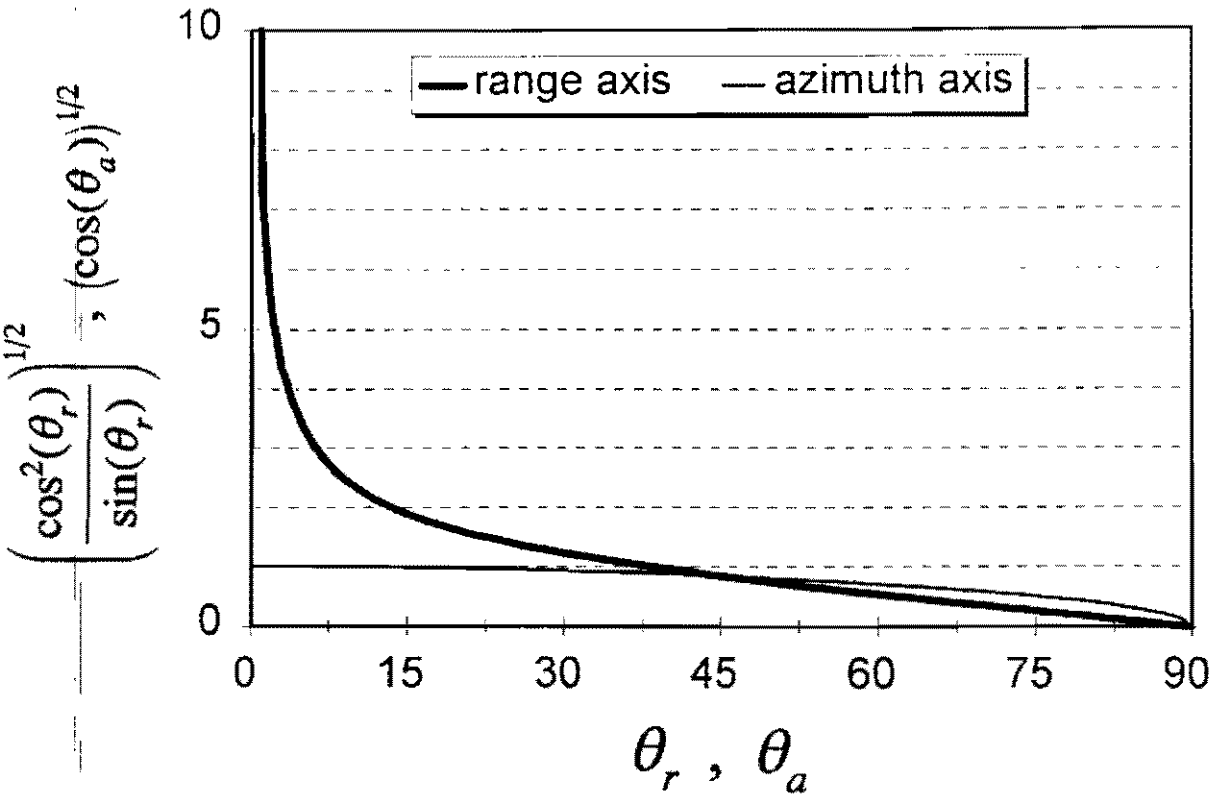
range axis
azimuth axis
10
5
0
0
15
30
45
60
75
90
θ_r , θ_a
$\left(\frac{\cos^2(\theta_r)}{\sin(\theta_r)}\right)^{1/2}$, $(\cos(\theta_a))^{1/2}$

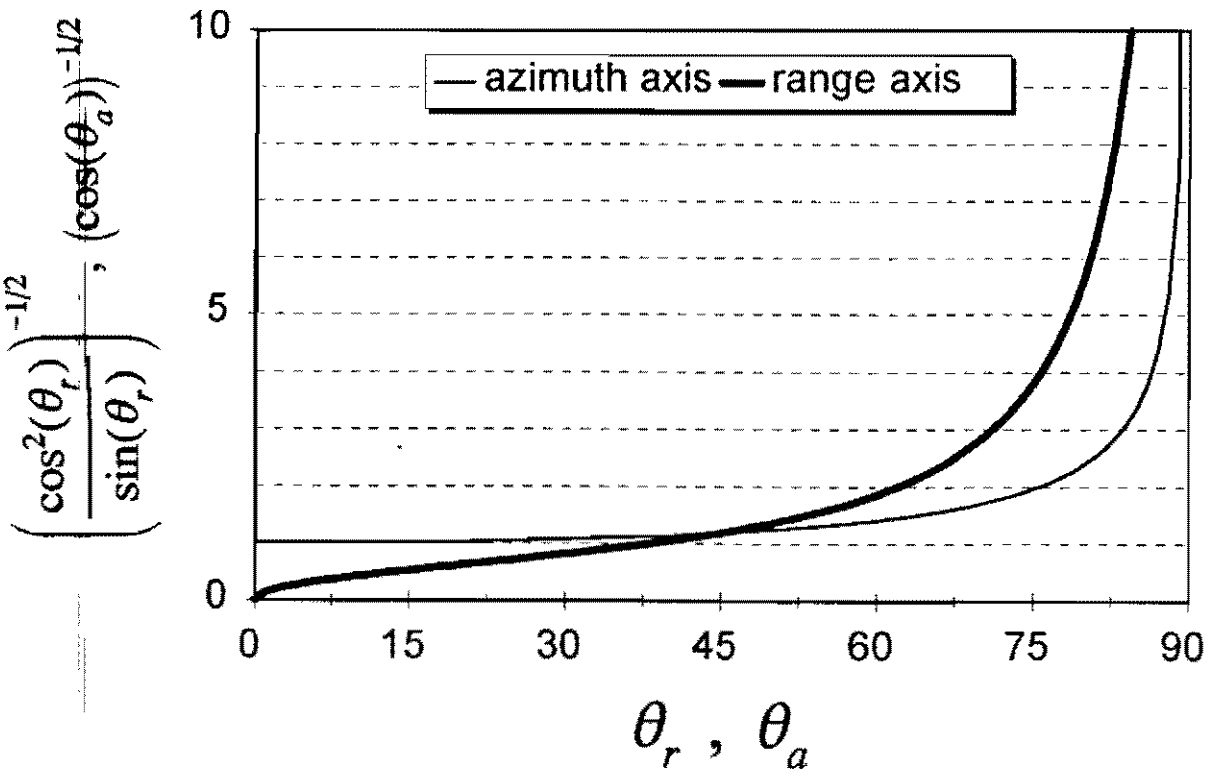
azimuth axis
range axis
10
5
0
0
15
30
45
60
75
90
θ_r , θ_a
$\left(\frac{\cos^2(\theta_r)}{\sin(\theta_r)}\right)^{-1/2}$, $(\cos(\theta_a))^{-1/2}$

Figure 4.

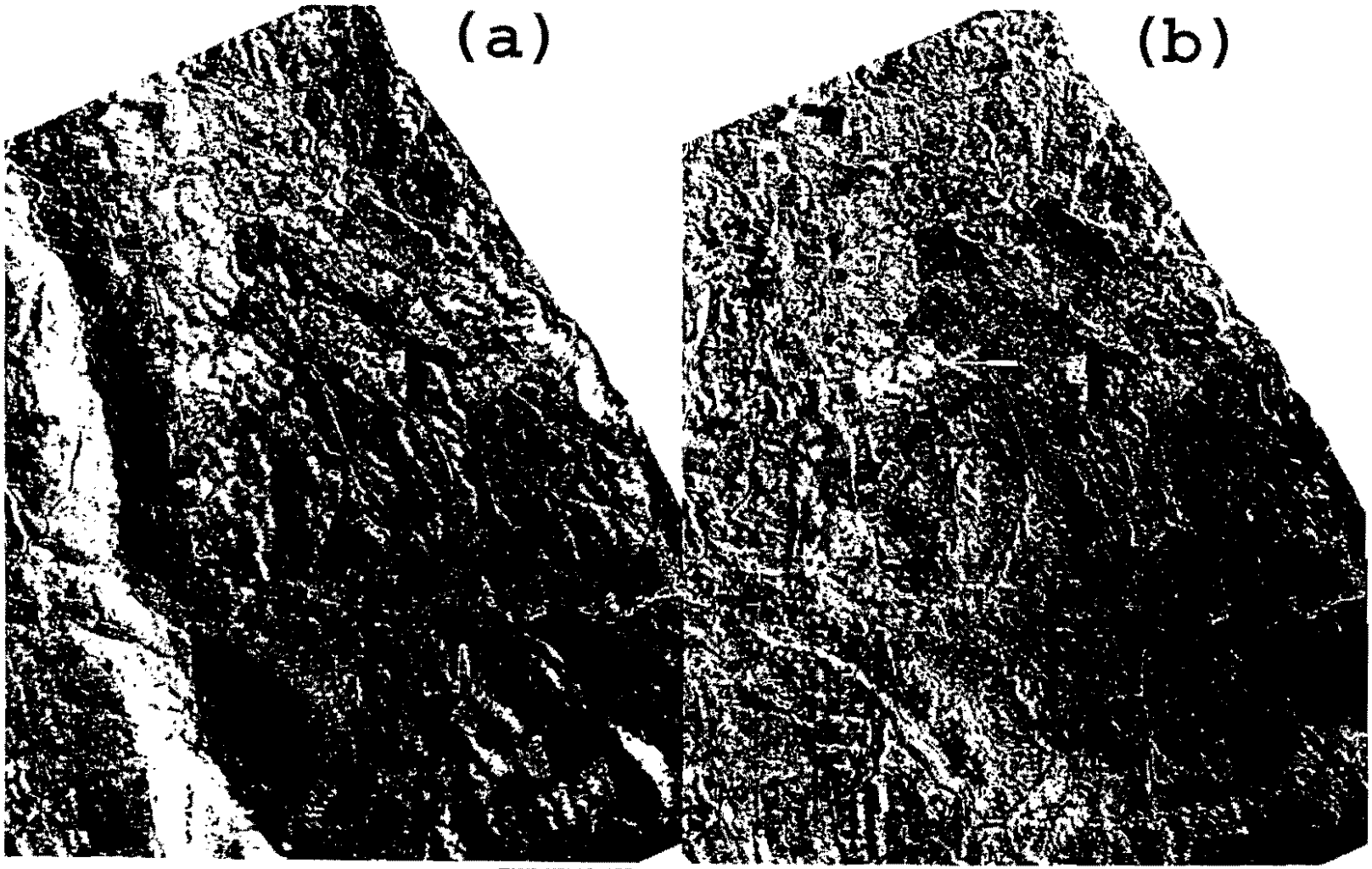

JUAN VINAS AREA. (A) RAW (B) CORRECTED

Figure 5